Microchimica Acta (2025) 192:408
https://doi.org/10.1007/s00604-025-07213-x

RESEARCH

Ultrasmall high-entropy alloy-nanolabels based immunochromatographic test strip for rapid, ultrasensitive, and catalytic detection of *Staphylococcus aureus*

Wei Huang[1] · Zhen Ren[2] · Xukui Li[2] · Rong Chen[3] · Dinglin Fan[1] · Jingjing Da[4] · Yan Zha[1,3,4] · Yongjie Xu[1,3]

Received: 24 February 2025 / Accepted: 1 May 2025

Abstract

The use of ultrasmall high-entropy alloys (HEAs, ≈5 nm) with unique catalytic properties, integrating them into lateral flow immunoassay (LFIA) for the detection of *Staphylococcus aureus* is proposed. Under optimal conditions, the detection limits of the HEAs-based LFIA were 1.5×10^3 CFU/mL via direct coloration and 15 CFU/mL using the DAB-enhanced catalytic signal, representing improvements of 10^3-fold and 10^5-fold, respectively. The HEAs demonstrated superior performance compared with traditional AuNPs, including enhanced sensitivity and high peroxidase activity (Km = 0.066 M, Vmax = 1.132×10^{-6} M min^{-1}), as well as excellent specificity and repeatability, with relative standard deviation (RSD) of less than 10%. Moreover, the incubation time for HEAs functionalized with antibodies to bind *Staphylococcus aureus* was only 5 min, compared with 20 min for functionalized AuNPs. The method also showed high specificity, effectively discriminating *Staphylococcus aureus* from other foodborne pathogens. The HEAs-based LFIA was successfully applied to food sample analysis, including milk and orange juice, demonstrating its robust applicability for real-world detection scenarios. This approach not only lowered the detection limit but also reduced the total detection time, making it a highly promising candidate for on-site detection of *Staphylococcus aureus* and other foodborne pathogens by simply changing the recognition element.

Keywords Lateral flow immunoassay · Foodborne pathogens · High-entropy alloys · Peroxidase-mimicking activity · On-site detection

Introduction

Staphylococcus aureus (*S. aureus*) is a common foodborne pathogen widely present in natural environments, including air, water and soil. Among foodborne pathogens, *S. aureus* stands out due to its high invasiveness and potent biological pathogenicity, causing severe health conditions such as pericarditis, pneumonia, purulent infections, toxic shock syndrome, and sepsis [1–3]. Its widespread presence in various food types makes *S. aureus* a major public health concern [4, 5]. There is an urgent need for the development of rapid, convenient, and highly sensitive detection methods for *S. aureus* [6]. However, traditional bacterial detection techniques, including bacterial culturing, polymerase chain reaction (PCR), and enzyme-linked immunosorbent assay (ELISA), are limited by complex sample preparation and the need for skilled operators [7, 8], which limit their practicality for point-of-care (POC) applications.

The lateral flow immunoassay (LFIA) offers significant advantages for the rapid, sensitive, and effective detection of pathogenic bacteria, owing to its user-friendly operation, fast response time, cost-efficiency, and visual readout capabilities [9–11]. As a result, LFIA has become a leading option for point-of-care (POC) testing and is widely utilized in applications such as clinical diagnostics, food

✉ Yan Zha
yanzhagz@126.com

✉ Yongjie Xu
504267611@qq.com

[1] Medical College, Guizhou University, Guiyang 550025, Guizhou, China

[2] NHC Key Laboratory of Pulmonary Immunological Diseases, Guizhou Provincial People's Hospital, Guiyang 550002, Guizhou, China

[3] Department of Laboratory Medicine, Guizhou Provincial People's Hospital, Guiyang 550002, Guizhou, China

[4] Renal Division, Department of Medicine, Guizhou Provincial People's Hospital, Guiyang 550002, Guizhou, China

Published online: 05 June 2025

safety, drug testing, and antibiotic residue [12, 13]. Traditional LFIA test strips primarily rely on colloidal gold nanoparticles (AuNPs) as colorimetric signal reporters, which allow for equipment-free detection and have been successfully commercialized [14, 15]. However, AuNPs-based LFIA systems are often limited by poor sensitivity and low quantification accuracy, making them inadequate for meeting the stringent requirements of food safety screening [16, 17]. To overcome these limitations, multifunctional nanomaterial-based LFIA have been developed, incorporating diverse signal mechanisms such as fluorescence [18], surface-enhanced Raman scattering [19] and photothermal signals [20], to enhance sensitivity. Despite their improvements, these approaches face challenges. Fluorescent sensors are susceptible to interference from internal and external variables, such as background noise, excitation source stability, and probe concentration [21]. SERS-based LFIA achieves up to a 1000-fold sensitivity improvement, but its reliance on bulky and expensive equipment limits its portability and broader adoption [22]. In photothermal approaches, their data acquisition and analysis times extend to 10–20 min, while ideal on-site evaluation need to complete within minutes [23]. Therefore, developing rapid and accurate detection methods for pathogenic bacteria remains crucial to ensuring human safety and public health.

High-entropy alloys (HEAs), consisting of five or more component elements in near equiatomic ratios, have recently gained widespread attention owing to their unique structural features, including the high-entropy effect, lattice distortion effect, slow diffusion effect and "the cocktail effect" [24]. These properties endow the HEAs with exceptional irradiation resistance [25], high strength [26], enhanced stability [27], high catalytic activity [28], and efficient photothermal conversion [29]. As a result, HEAs are considered strong candidates for applications in energy systems [30–32], therapeutics [33], and various other fields [34]. Compared with single, bimetallic catalysts or medium-entropy alloys, the multi-component adjustability of HEAs can provide different desired active sites, endowing them with a new class of catalytic materials across various research fields [35, 36]. For instance, HEAs are viewed as promising electrocatalytic catalysts [37, 38]. Specifically, "the cocktail effect" resulting from multiple transition metals dopant can significantly alter the local environment of active center, resulting in HEAs with superior catalytic properties due to interatomic d-band ligand effects or crystal lattice strain effects [39]. To date, most research on HEAs has focused on their uses as metallic structural materials, improving properties such as hardness, elastic modulus, shear modulus, tensile strength, radiation resistance, and thermal expansion coefficient [40]. However, studies on HEAs-based LFIA for detecting foodborne pathogens and other biomarkers remain scarce. Additionally, HEAs are frequently synthesized through mechanical alloying synthesis and fast-moving bed pyrolysis, involving high temperatures and extended processing times [41], which limits their practicality to some extent. Therefore, it is necessary to develop a new approach for rapid, simple and cost-effective preparation of HEAs and expand their application range.

In this work, we present a general one-pot low-temperature reduction-diffusion strategy to synthesize ultrasmall AuPtIrRuRh HEAs and integrate them into LFIA for the rapid and cost-effective detection of *Staphylococcus aureus*. The HEAs were electrostatically conjugated with anti-*S. aureus* antibodies to create an ultra-sensitive probe with high catalytic activity, eliminating the need for cross-linking agents. Three forms of LFIA systems were systematically developed and compared: LFIA based on AuNPs, LFIA using HEAs, and an enhanced HEAs-based LFIA leveraging the peroxidase-like activity of HEAs. Conventional AuNPs served as a reference to highlight the superior sensitivity of HEAs over conventional AuNPs-based LFIA. The HEAs-mediated LFIA demonstrated high accuracy, improved sensitivity, a straightforward design, and rapid detection capabilities. This approach establishes a highly promising and innovative strategy for the detection of *S. aureus*, with potential adaptability to other pathogens by modifying the recognition elements.

Experimental section

Materials and reagents

Trisodium citrate ($C_6H_5Na_3O_7$), $HAuCl_4{\cdot}3H_2O$, Tween-20, tris-(hydroxymethyl) aminomethane (Tris), DNase/RNase-free water, and Sodium chloride (NaCl) were purchased from Sangon Biotechnology Inc. (Shanghai, China). The sample, absorption, and backing layers were ordered from JieYi (Shanghai, China), and nitrocellulose membranes (CN95) were acquired from Sartorius (Gottingen, Germany). $NaPtCl_6{\cdot}6H_2O$ was ordered from Sigma-Aldrich (Merck KGaA, Germany), while $Na_3IrCl_6{\cdot}XH_2O$ was supplied by Damas-beta (Shanghai, China). K_3RhCl_6 and $K_2RuCl_5(H_2O)$ were obtained from Aladdin (Shanghai, China). The rabbit monoclonal antibody (mAb) against *S. aureus* was received from Biodragon (Suzhou, China), while the polyclonal antibody (pAb) against *S. aureus* and goat anti-rabbit IgG were supplied by Bioss (Beijing, China). Sucrose and Potassium carbonate (K_2CO_3) were provided by Zhi Yuan Reagent Co, Ltd (Tianjin, China). Bovine albumin (BSA) was acquired from Beyotime (Shanghai, China) and PBS was purchased from Boerlab (Chongqing, China).

The metal enhanced 3,3′-Diaminobenzidine tetrahydrochloride (DAB) substrate Kit was supplied by Solarbio (Beijing, China). The single-component 3,3′,5,5′-tetramethylbenzidine (TMB, > 99%) substrate solution containing H_2O_2 was sourced from Beyotime Biotechnology (Shanghai, China). $NaBH_4$ was obtained from Aladdin (Shanghai, China).

Apparatus

An HM3035XYZ platform dispenser was used to prepare the test and control lines (Shanghai Kinbio Technology. Co., Ltd. Shanghai, China). The CTS300 automatic programable cutter was purchased from Jinbiao Biotechnology Co., Ltd. (Shanghai, China). The color intensity was measured using a GIC-H1 portable colloidal gold immunoassay analyzer (Suzhou Hemai Precision Instrument Co., Ltd.).

Mass spectrometry analysis was characterized by Microflex LT/SH (Karlsruhe, Germany). Scanning electron microscope (SEM) was performed using a Zeiss Gemini 300 instrument (Zeiss, Gemini). High resolution transmission electron microscopy (HRTEM) images and Energy-dispersive spectroscopy (EDS) images were characterized by SU8010 Hitachi (Hitachi, Japan). The Microplate Reader was used to measure the absorbance change of the reaction system (BioTek, USA).

Preparation of gold nanoparticles, high-entropy alloys, and others

Based on existing literature, AuNPs were synthesized following a previously established method with slight modifications [42]. Initially, a flask was supplied with 16 mL of a 0.25% $HAuCl_4$ stock solution followed by adding DNase/RNase-free water to achieve a total volume of 200 mL. The solution was heated to boiling with mechanical stirring. Subsequently, 12 mL of a 1% (w/w) aqueous sodium citrate solution was quickly added. After boiling continuously for 15 min, during which the solution's color shifted from transparent to deep burgundy-red, heating was stopped, and stirring continued for an additional 15 min. Ultimately, the colloidal solution was adjusted back to the initial volume of 200 mL by adding DNase/RNase-free water, and the colloidal solution was stored at 4 °C for subsequent applications.

The AuPtIrRuRh HEAs were synthesized using a low-temperature reduction-diffusion strategy. The precursor solution was prepared by adding 1% $HAuCl_4{\cdot}3H_2O$, $NaPtCl_6{\cdot}6H_2O$, $Na_3IrCl_6{\cdot}XH_2O$, K_3RhCl_6, $K_2RuCl_5{\cdot}(H_2O)$ to 40 mL of H_2O. The resulting mixture was sonicated in an ice-water bath for 2 min, followed by the addition of 2 mL $NaBH_4$ (2 mg/mL). The mixture was mechanically stirred at 7000 rpm for 5 min, resulting in the formation of single-phase HEAs through the combined processes of reduction and atomic diffusion. The HEAs solution was stored at 4 °C. Using this same method, Au-PtNPs, Au-Pt-IrNPs, Au-Pt-Ir-RuNPs were also synthesized. The prepared AuNPs were characterized by scanning electron microscopy (SEM). The HEAs were characterized by high-resolution transmission electron microscopy (HRTEM) and energy-dispersive spectroscopy (EDS).

Catalytic activity test

The catalytic activities of AuNPs, Au-PtNPs, Au-Pt-IrNPs, Au-Pt-Ir-RuNPs, and HEAs were evaluated by monitoring color changes in TMB and DAB using a Microplate Reader across a wavelength range of 300–800 nm. For the HEAs colorimetric detection assay, 100 µL of TMB or DAB solution was mixed with 100 µL of HEAs and incubated for 5 min at 37 °C. Oxidized TMB or DAB sediment was yielded by the reaction solution for color analysis. The absorbance was measured from 300 to 800 nm.

Peroxidase-like activity evaluation

Place 100µL of a solution containing various amounts (from 1 to 20 µg) of peroxidase nanozyme in 0.2 M NaAc–HAc buffer, pH 3.6, into separate tubes. Add 50 µL of TMB solution (10 mg mL^{-1} in DMSO) to each tube and mix thoroughly. Incubate the reaction mixture in a thermostatic water bath in the dark at a temperature of 37 °C for 5 min. After incubation, add H_2O_2 to the reaction mixture to achieve a final concentration of 1 M, and measure the colorimetric response by absorbance at 652 nm every 10 s for up to 400 s after H_2O_2 addition. The peroxidase-like activity (b, U) was calculated by the Eq. (1) [43]:

$$b = \frac{V}{\varepsilon \times L} \times \frac{\Delta A}{\Delta t} \quad (1)$$

where $b_{nanozyme}$ represents the catalytic activity of nanozyme expressed in units. One unit is defined as the amount of nanozyme that catalytically produces 1 µmol of product per min at 37 °C; V is the total volume of reaction solution (µL); ε is the molar absorption coefficient of the colorimetric substrate, which is typically maximized at 39,000 M^{-1} cm^{-1} at 652 nm for TMB; L is the path length of light traveling in the cuvette (cm); A is the absorbance after subtraction of the blank value; and ΔA/Δt is the initial rate of change in absorbance at 652 nm min^{-1}. Further, the specific activity (a, U mg^{-1}) can be calculated by the Eq. (2) [43]:

$$a_{nanozyme} = {}^{b_{nanozyme}}/_{[m]} \quad (2)$$

where $a_{nanozyme}$ is the specific activity expressed in units per milligram (U mg^{-1}) nanozymes, and [m] is the nanozyme weight (mg) of each assay.

Steady-state dynamic parameter measurement

Steady-state kinetic assays were conducted in HAc-NaAc buffer (0.1 M, pH 3.6) containing HEAs (35 μg mL^{-1}) and varying concentrations of TMB (0.125 to 0.75 mM), with a fixed concentration of H_2O_2 (1 M). All reactions were monitored by measuring the oxidation of TMB at 652 nm every 10 s. The catalytic kinetic parameters (Km and Vmax) were then determined from Lineweaver–Burk plots, which were derived from the double inverse form of the Michaelis–Menten Eq. (3) [43]:

$$\frac{1}{V} = \frac{K_m}{V_{\max}} \times \frac{1}{[S]} + \frac{1}{V_{\max}} \quad (3)$$

where V is the initial velocity, V_{max} is the maximal reaction rate, [S] is the concentration of substrate, and Km is the Michaelis constant.

Modification of AuNPs and high-entropy alloys

AuNPs were thoroughly mixed with a K_2CO_3 solution, and 5 μL of anti-*S. aureus* IgG was added to reach a final concentration of 5 μg/mL. The mixture was shaken on a mixer for 60 min, followed by the addition of bovine serum albumin (BSA) at a final concentration of 0.1% (w/v) as a blocking agent, and then shaken for 30 min at room temperature. The mixture was then centrifuged at 10,000 rpm for 12 min to collect a red pellet of anti-*S. aureus* IgG-modified AuNPs, which was resuspended in PB solution (10 mM, pH 7.35) containing 2% sucrose, 1% BSA, and 0.05% Tween-20, resulting in AuNPs-pAb probes for further applications.

To achieve specific lateral flow immunoassay and precise bacterial recognition, we conjugated anti-*S. aureus* IgG, a rabbit IgG, to the HEAs solution via electrostatic interactions. The detailed procedure is as follows: 40 μL of BSA (1%, w/v) was added to 1 mL of HEAs solution and the mixture was shaken at room temperature for 30 min. Subsequently, K_2CO_3 and 5 μL of polyclonal antibody (pAb) (1 mg/mL) were added to the solution with continuous shaking for 1 h. The mixture was then centrifuged at 8,000 rpm for 15 min and resuspended in PB solution for further applications.

Fabrication of lateral flow immunoassay strip

The sample pads were immersed in 0.05 M Tris–HCl (pH 8.0) buffer containing 0.15 M NaCl and 0.25% Tween-20 (v/v) for 1 h, then dried at 37 °C overnight. The test line (T-line) and control line (C-line) were generated by dispensing anti-*S. aureus* IgG (2.5 mg/mL) and goat anti-rabbit IgG (1 mg/mL) onto the NC membrane, respectively. The absorbent pads and sample pads were sequentially assembled onto a PVC backing plate, with an approximate 2 mm gap from the NC membrane. The assembled strips were cut to a width of 2.5 mm to complete the construction of the LFIA.

High-entropy alloys-based LFIA detection

Five microliters of HEAs-pAb probe was added to the sample solution containing target bacteria and allowed to react for 5 min in a phosphate buffer (PB) solution containing NaCl and 0.04% Tween-20. Then, the reaction solution was introduced onto the sample pad of the LFIA. After running for 10 min under capillary force, the colorimetric results were recorded. Following the addition of a DAB mixed solution to the T-line directly, the catalytic signal on the T-line was amplified, and the images were captured via a smartphone. Finally, the GIC-H1 portable colloidal gold immunoassay analyzer was used for the quantitative analysis of the gray value on the T-line.

Bacterial strain culture

Standard strains, including *S. aureus* (ATCC 29213 and ATCC 25923) and additional clinical bacterial isolates (*P. aeruginosa, S. epidermidis, E. coli,* and *E. faecium*) were obtained from the Microbiology Laboratory of Guizhou Provincial People's Hospital (Guizhou, China). The use of clinical bacterial isolates was approved by the Ethics Committee of Guizhou Provincial People's Hospital (No. [2024]171). These strains were cultivated on Columbia blood agar and incubated at 35 °C with 5% carbon dioxide for 24 h.

Determination of S. aureus in food samples

In order to explore the applicability of the established HEAs-based LIFA sensor in real sample analysis, *S. aureus* was introduced into milk and orange juice samples. Each 1 mL sample of milk or orange juice was spiked with 9×10^8 CFU of *S. aureus* and mixed well. Then 50 μL of milk or orange juice mixture was transferred to the sample pad of the LFIA immunosensor and its signal response on the T-line was recorded. All tests were performed in quintuplicate.

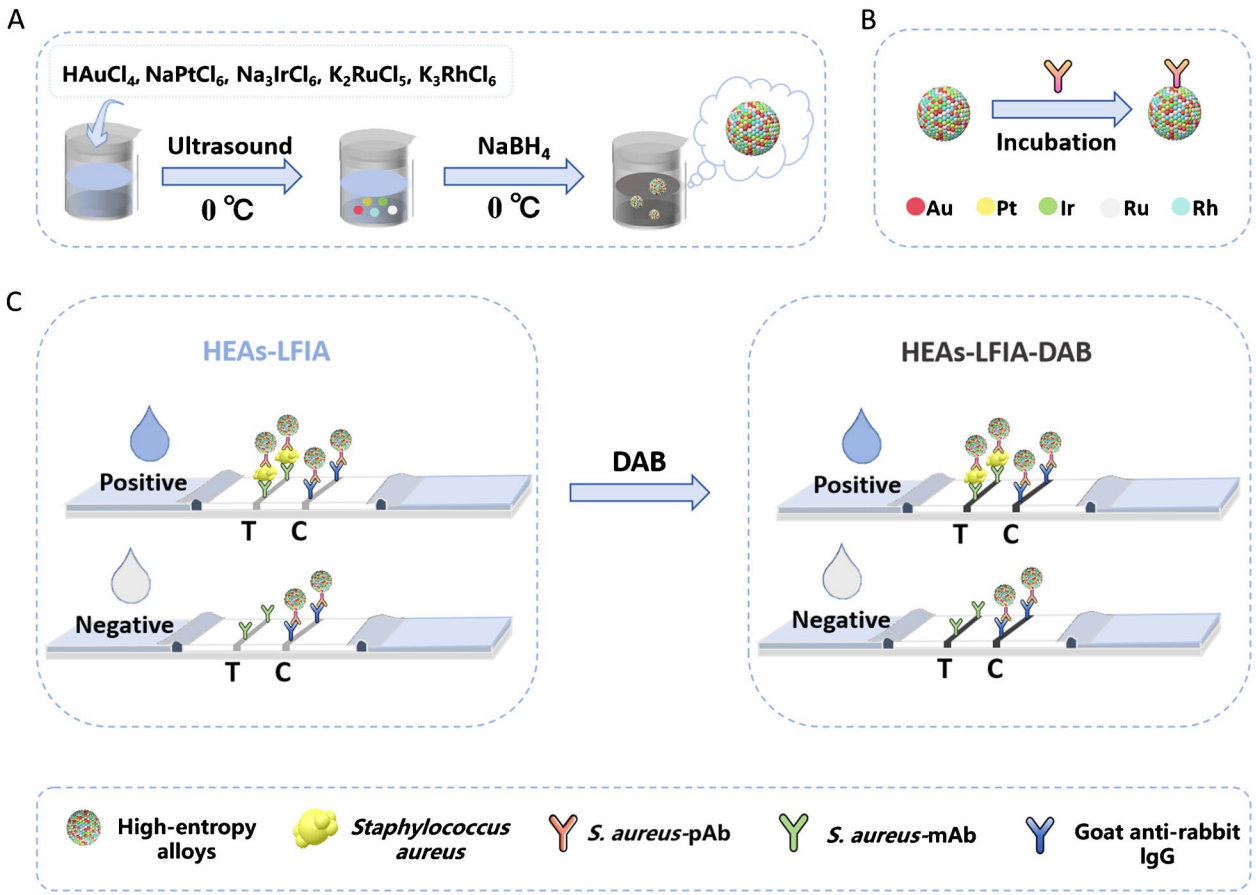

Scheme 1 Schematic representation of the multifunctional HEAs-based LFIA for *S. aureus* detection. **A** Synthesis process of HEAs using a low-temperature reduction-diffusion strategy. **B** Preparation of antibody-modified HEAs via electrostatic interaction between HEAs and anti-*S. aureus* pAb. **C** Mechanism of LFIA detection, including the generation of T-line and C-line signals and DAB-based signal amplification for enhanced sensitivity

Results and discussion

Principle of high-entropy alloys-pAb-mediated LFIA for S. aureus detection

The detection principle of the high-entropy alloys (HEAs)-pAb-mediated lateral flow immunoassay (LFIA) is based on a sandwich-like LFIA model, as illustrated in Scheme 1. HEAs were synthesized via a low-temperature reduction-diffusion strategy, with the synthesis process shown in Scheme 1A. The precursor solution was subjected to sonication in an ice-water bath, followed by the addition of a reducing agent. Anti-*S. aureus* polyclonal antibodies (pAb) were then conjugated to the HEAs solution through electrostatic interactions (Scheme 1B). The working principle of the LFIA is outlined in Scheme 1C. The test line (T-line) and control line (C-line) were prepared by dispensing anti-*S. aureus* IgG (2.5 mg/mL) and goat anti-rabbit IgG (1 mg/mL) onto the nitrocellulose (NC) membrane, respectively. In the presence of *S. aureus*, the pathogen binds to the recognition sites on the HEAs-pAb probe, resulting in the accumulation of the nanoprobe at the T-line and an increase in T-line color intensity corresponding to the increasing concentration of *S. aureus*. To further amplify the signal and enhance the detection sensitivity, a DAB solution was applied to the test area. Due to the strong catalytic activity of the HEAs, the initial gray band transitioned into a distinct brown band. In the absence of *S. aureus*, the HEAs-pAb probe can be captured by goat anti-rabbit IgG (1 mg/mL) when they migrate upward along the strip, resulting in coloration of the control line (C-line). The C-line remained visible in all cases, serving as a functional indicator of the LFIA's reliability. The entire LFIA detection process could be visually assessed within 10 min. Quantitative analysis was achieved using a GIC-H1 portable colloidal gold immunoassay analyzer, allowing for accurate measurement without specialized personnel or advanced equipment.

Characterization of AuNPs and high-entropy alloys

As shown in Fig. 1A, the colloidal gold solution prepared by citrate reduction exhibited a distinct red color. The TEM and SEM images of gold nanoparticles displayed a well-dispersed spherical structure with an approximate diameter of 13 nm in Fig. 1B and Fig. 1C. As seen in Fig. 1D, the ultrasmall high-entropy alloys were synthesized using a low-temperature reduction-diffusion strategy, exhibiting an ash-black solution without sediment. The morphology of the resulting AuPtIrRuRh HEAs was revealed by high-resolution TEM (HRTEM), disclosing a distinct elliptical structure as illustrated in Fig. 1E, and the size distribution of the HEAs was approximately 5 nm. As shown in Fig. 1F, the element maps by energy-dispersive X-ray spectroscopy (EDS) suggested that all the elements were uniformly distributed in the HEAs. To synthesize stable high-entropy alloys via a simple one-pot strategy, the preparation temperature was systematically investigated. As displayed in Fig. 1G, no sediment was observed in the solution at a preparation temperature of 0 °C, while sedimentation occurred at 4 °C and 25 °C. The catalytic activities of nanoparticles synthesized at these temperatures were compared (Fig. 1H), and the results demonstrated that nanoparticles prepared at temperatures of 0°C exhibited greater uniformity, a higher concentration of generated nanoparticles, and enhanced catalytic activity. Thus, 0 °C was determined to be the optimal temperature for synthesizing high-entropy alloys in this assay.

Catalytic properties of high-entropy alloys

Several control experiments were conducted to elucidate the catalytic activity of high-entropy alloys in this study. TMB and DAB were added to various nanoparticle solutions, including AuNPs, Au-PtNPs, Au-Pt-IrNPs, Au-Pt-Ir-RuNPs and HEAs. As illustrated in Fig. 2A, after the addition of the TMB system, the absorbance and color intensity of HEAs (tube e) were significantly greater than those observed in the AuNPs (tube a), Au-PtNPs (tube b), Au-Pt-IrNPs (tube c), and Au-Pt-Ir-RuNPs (tube d), exhibiting exceptional peroxidase-mimicking activity. Additionally, as seen in Fig. 2B, after the addition of the DAB system, HEAs (tube e) produced distinct dark brown sediment without an observable absorption peak, further confirming the superior catalytic activity of HEAs compared to other nanoparticles tested.

To further investigate the catalytic efficiency, apparent steady-state kinetic analyses were conducted for AuNPs, Au-PtNPs, Au-Pt-IrNPs, Au-Pt-Ir-RuNPs, and HEAs. Several key parameters, including the maximum reaction rate (Vmax) and the Michaelis–Menten constant (Km), were evaluated by constructing Michaelis–Menten equations for different TMB concentrations. Figure 3A illustrated the reaction-time curves of TMB colorimetric reaction catalyzed

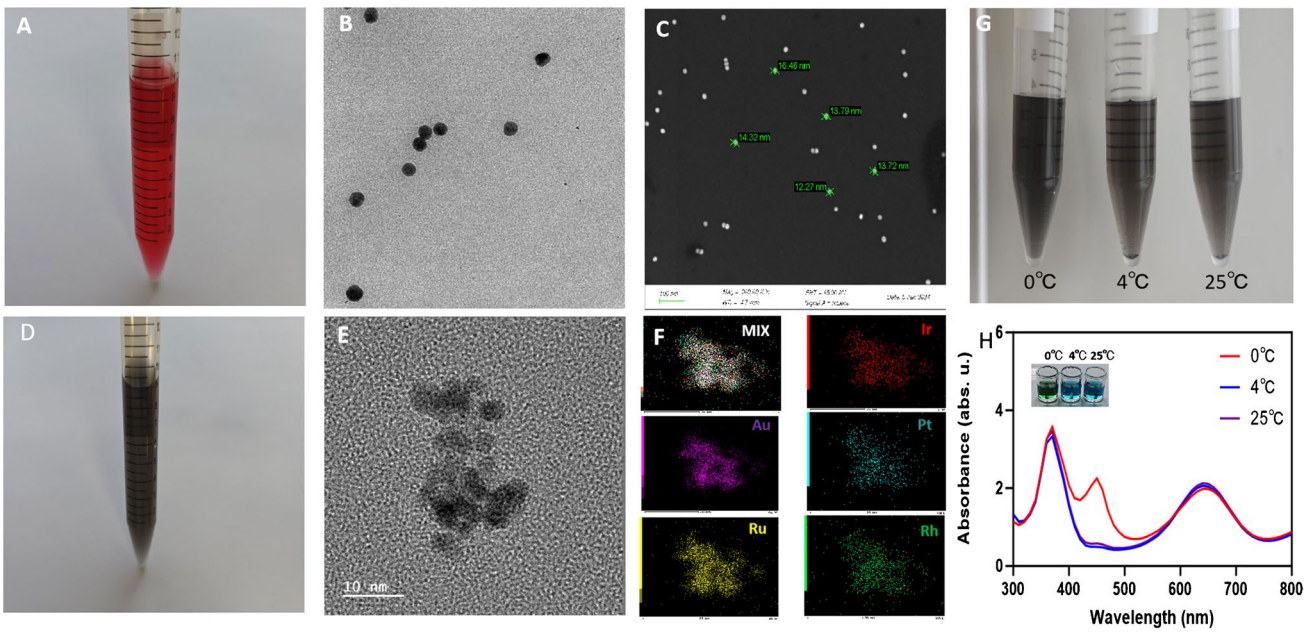

Fig. 1 Characterization of colloidal gold and high-entropy alloys. **A** Colloidal gold solution prepared via citrate reduction. **B** TEM image of colloidal gold nanoparticles. **C** SEM image of colloidal gold nanoparticles. **D** High-entropy alloys (HEAs) solution synthesized using a low-temperature reduction-diffusion strategy. **E** High-resolution TEM (HRTEM) image of HEA. **F** Elemental mapping results of HEAs by energy-dispersive X-ray spectroscopy (EDS). **G** The effect of preparation temperature (0 °C, 4 °C, 25 °C) on HEA stability. **H** Comparison of catalytic activities of HEAs synthesized at different temperatures (0 °C, 4 °C, 25 °C)

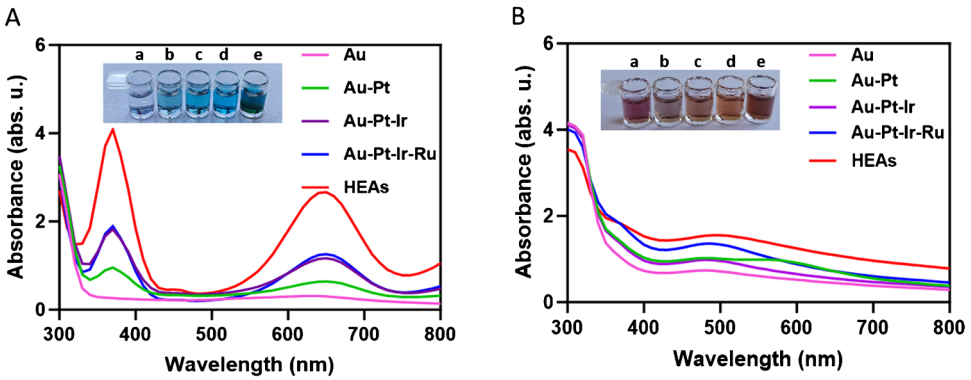

Fig. 2 Comparison of the catalytic activity of various nanoparticles using TMB and DAB substrates. **A** Catalytic activity comparison using the TMB substrate, demonstrating the superior catalytic performance of HEAs (tube e) compared to AuNPs (tube a), Au-PtNPs (tube b), Au-Pt-IrNPs (tube c), and Au-Pt-Ir-RuNPs (tube d). **B** Catalytic activity comparison using the DAB substrate, where HEAs (tube e) exhibited a distinct dark brown sediment, further highlighting their superior catalytic activity over AuNPs (tube a), Au-PtNPs (tube b), Au-Pt-IrNPs (tube c), and Au-Pt-Ir-RuNPs (tube d)

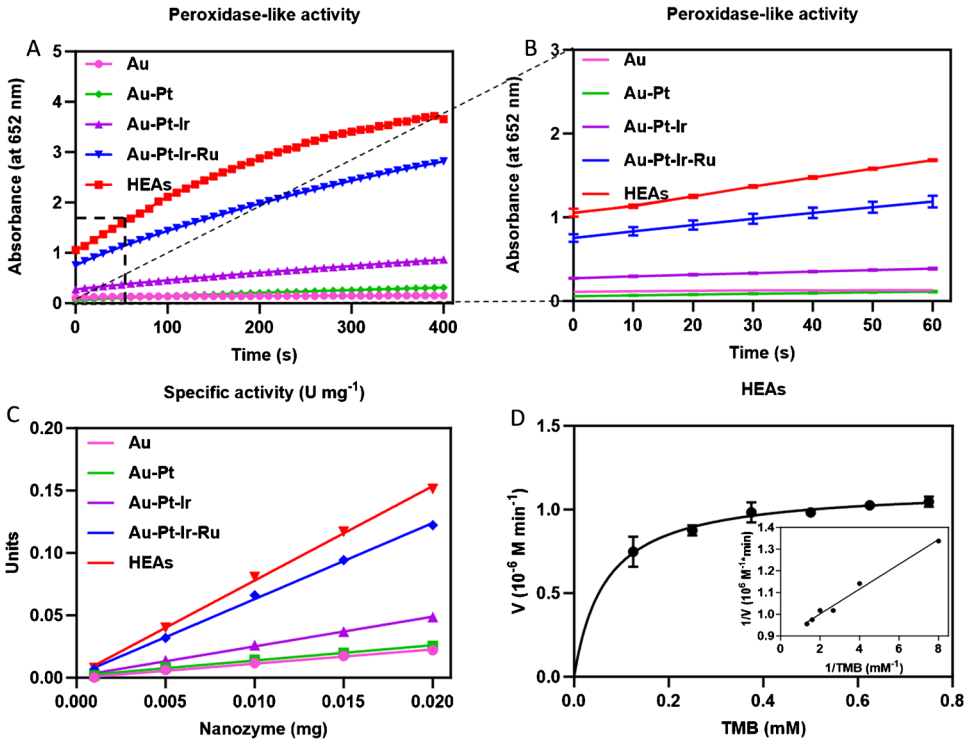

Fig. 3 **A** Reaction-time curves of the TMB colorimetric reaction catalyzed by AuNPs, Au-PtNPs, Au-Pt-IrNPs, Au-Pt-Ir-RuNPs and HEAs in 400 s. **B** Magnified initial linear portion of the nanozyme reaction-time curves. **C** Specific activity of AuNPs, Au-PtNPs, Au-Pt-IrNPs, Au-Pt-Ir-RuNPs and HEAs. **D** Enzymatic kinetics fitting curve and double-reciprocal fitting curve of HEAs for TMB

by AuNPs, Au-PtNPs, Au-Pt-IrNPs, Au-Pt-Ir-RuNPs and HEAs nanozymes over 400 s. As shown in Fig. 3B, the magnified initial linear portion of the reaction-time curves was analyzed. A length of 60 s was chosen for the initial rate period because the R^2 coefficients were close to 1 during this period after a linear regression analysis. The initial reaction rates were measured at different concentrations of AuNPs, Au-PtNPs, Au-Pt-IrNPs, Au-Pt-Ir-RuNPs and HEAs for H_2O_2-TMB reaction. As displayed in Fig. 3C, the specific activity of HEAs was calculated to be 7.567 U/mg, indicating superior enzyme activity compared to the other nanoparticles (6.099 U/mg for Au-Pt-Ir-RuNPs, 2.383 U/mg for Au-Pt-IrNPs, 1.227 U/mg for Au-PtNPs, 1.143 U/mg for AuNPs). As seen in Fig. 3D, the Km and Vmax of the TMB-based peroxidase-mimetic enzyme in HEAs were 0.066 M and 1.132×10^{-6} M min^{-1}, respectively. Compared to the catalytic kinetic performance of AuNPs (Km: 0.062 M, Vmax: 3.511×10^{-6} M min^{-1}), Au-PtNPs (Km: 0.186 M, Vmax: 1.223×10^{-6} M min^{-1}), Au-Pt-IrNPs (Km: 0.205 M, Vmax: 1.671×10^{-6} M min^{-1}), Au-Pt-Ir-RuNPs (Km: 0.111 M, Vmax: 1.199×10^{-6} M min^{-1}), respectively, HEAs exhibited high catalytic activity (Fig. S7). These results indicated

that HEAs hold significant potential as a high-performance label for signal amplification on the LFIA platform.

Feasibility of LFIA based on high-entropy alloys for S. aureus detection

To verify the conjugation of nanoparticles with pAbs, the stability of nanoparticle before and after functionalization was evaluated by monitoring color changes in a salt solution (Fig. 4). And the corresponding changes of UV–Vis spectroscopy were recorded by using a microplate reader. In the assay, 200 µL of AuNPs and HEAs solution was mixed with different concentrations of NaCl solution. As illustrated in Fig. 4A, when the gold nanoparticles were not conjugated to antibodies, the addition of salt (40 mmol/L in tube b, 80 mmol/L in tube c, and 120 mmol/L in tube d) caused the color transition of nanoparticles solution from red to blue, accompanied by a decrease in absorbance. In contrast, the gold nanoparticles conjugated with antibodies have no changes in the solution's color and absorbance after adding salt solutions. Furthermore, the AuNPs-pAb conjugates can be captured by goat anti-rabbit IgG (1 mg/mL) when they migrate upward along the strip, resulting in a red line on the strip (f') as illustrated in

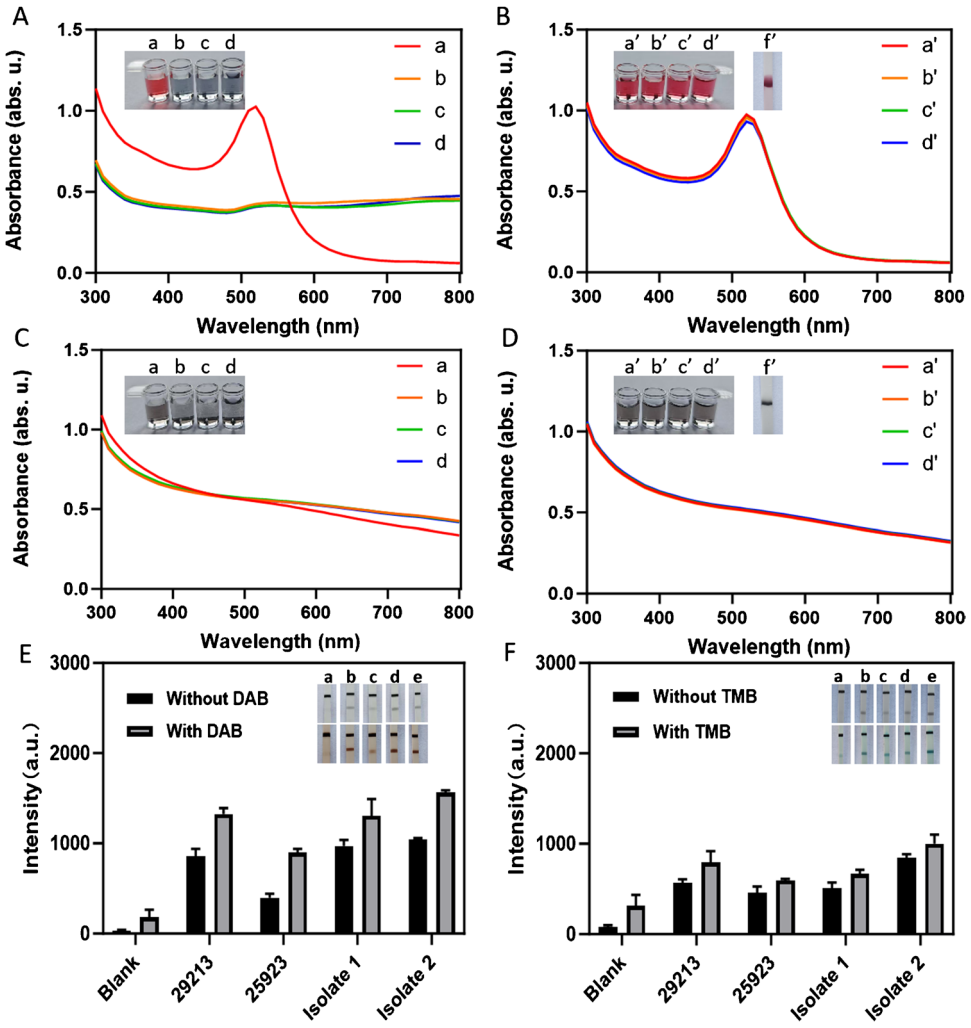

Fig. 4 Verify the conjugation of gold nanoparticles and HEAs with pAb's. **A** Changes in the color and absorbance of colloidal gold solutions. **B** Changes in the solution color and absorbance of colloidal gold conjugated with pAb's and the capture situation of the functionized nanoparicles on the test strip. **C** Changes in the color and absorbance of high-entropy alloys solutions. **D** Changes in the solution color and absorbance of high-entropy alloys conjugated with pAb's, and the capture situation of the functionized nanoparicles on the test strip. (a and a':0 mmol/L, b and b':40 mmol/L, c and c':80 mmol/L, d and d':120 mmol/L, f':Au-pAb probe and HEAs-pAb probe were captured by goat anti-rabbit IgG on the test strip). Feasibility of the HEAs-pAb probe for detecting various bacteria verified by visual observation and corresponding catalytic signals. **E** Catalytic signals of DAB substrate, showing rapid and strong signal development. **F** Catalytic signals of TMB substrate, with slightly slower and weaker signal development (a: Blank; b: S. aureus ATCC 29213; c: S. aureus ATCC 25923; d: Clinical bacterial isolate-1; e: Clinical bacterial isolate-2)

Fig. 4B. These results confirmed the successful conjugation of gold nanoparticles with antibodies. Similarly, the stability of HEAs before and after conjugation with pAb's was tested. Althogh the absorbance of the HEAs solution has negligible chang after the addition of salt in Fig. 4C, precipitation can be significantly observed. After the addition of salt solution, the HEAs-pAb conjugates are still stable and generate little precipitation in Fig. 4D. And the HEAs-pAb probes can be immobilized by goat anti-rabbit IgG as they migrated upward along the strip, resulting in a black line on the strip (f'). These results further indicated the successful conjugation of HEAs with antibodies.

To evaluate the feasibility of the HEAs-pAb probe-based lateral flow test strips, a comparative assay was performed using standard bacterial strains and clinical isolates. Figure 4E and F illustrated the effectiveness of LFIA employing high-entropy alloys for *S. aureus* detection, along with catalytic responses using DAB and TMB. Under the DAB system, color development occurred within approximately 1 min, while TMB required about 5 min. Furthermore, the DAB system generated a stronger signal than TMB, leading to the selection of DAB as the substrate for subsequent test strip experiments.

Experimental optimization of LFIA based on AuNPs and high-entropy alloys

To develop rapid and accurate LFIA sensors, parameters related to detection conditions were systematically optimized, including the volume of K_2CO_3, the concentration of NaCl, and the incubation time of HEAs-pAb or AuNPs-pAb probes with bacteria. Optimal testing conditions were identified when the colorimetric intensity of both the C-line and T-line reached stability. All parameters were optimized using *S. aureus* ATCC 29213 as a model bacteria. The volume of K_2CO_3 was first optimized, as it directly affected the coupling efficiency of HEAs or AuNPs with anti-*S. aureus* IgG, influencing key parameters within the LFIA system. As illustrated in Fig. 5A and Fig. 5B, the signal intensity of AuNPs or HEAs increased as the volume of K_2CO_3 ranged from 0 to 20 µL, but decreased at 25 µL. This reduction in intensity was likely due to excess K_2CO_3 inhibiting the binding between anti-*S. aureus* antibodies and AuNPs or HEAs. Consequently, a K_2CO_3 volume of 20 µL was selected for further experiments. Moreover, NaCl concentration, critical for HEAs-pAb probe and *S. aureus* binding, was then optimized. As depicted in Fig. 5C and Fig. 5D, the signal intensity peaked at 80 mmol/L, then declined beyond this point.

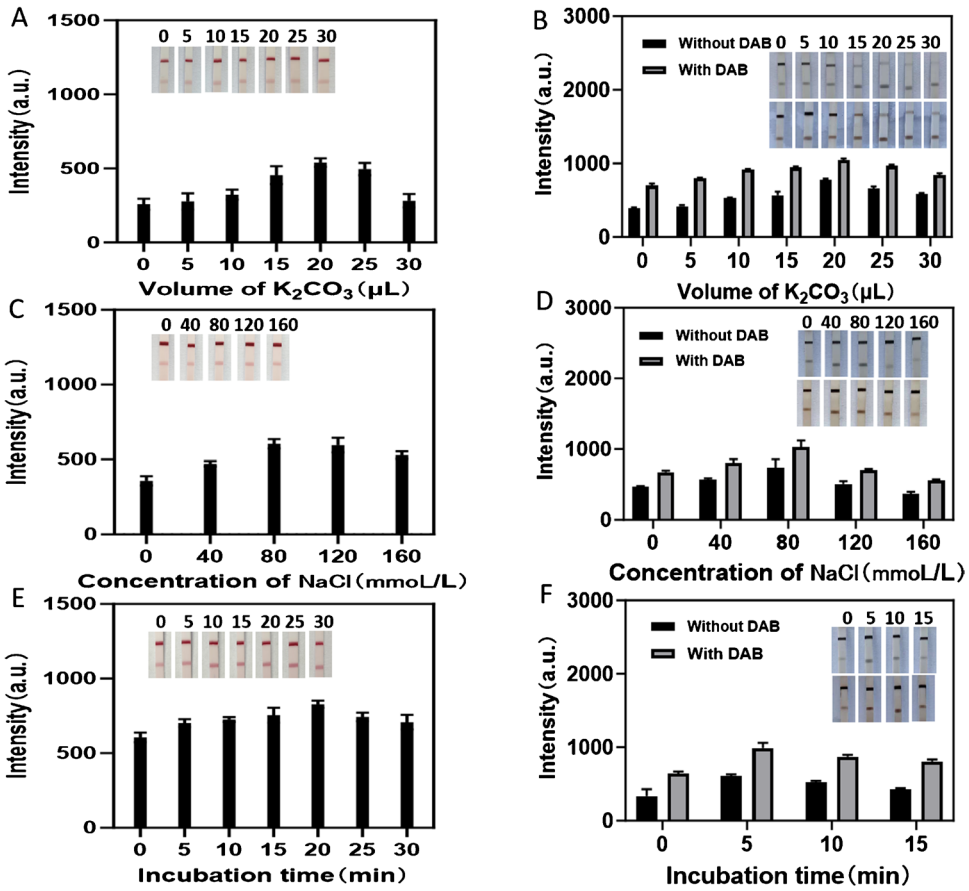

Fig. 5 Optimization of experimental parameters. **A** Volume of K_2CO_3 required for conjugating AuNPs with anti-*S. aureus* IgG. **B** Volume of K_2CO_3 required for conjugating HEAs with anti-*S. aureus* IgG. **C** NaCl concentration required for optimal binding between AuNPs-pAb probes and bacteria. **D** NaCl concentration required for optimal binding between HEAs-pAb probes and bacterial IgG. **E** Incubation time required for AuNPs-pAb probes and bacterial binding. **F** Incubation time required for HEAs-pAb probes and bacterial IgG

This decrease may result from excessive salt concentration compromising the integrity of *S. aureus*, and weakening HEAs-pAb probe and *S. aureus* binding. Thus, 80 mmol/L of NaCl was adopted for subsequent experiments. Finally, the incubation time of AuNPs-pAb or HEAs-pAb and *S. aureus* was evaluated. Figure 5E and F indicated that the optimal incubation time was 20 min for AuNPs-pAb, while HEAs-pAb required only 5 min to achieve distinct signal intensity. Accordingly, incubation times of 20 min and 5 min were selected for these subsequent experiments.

Sensitivity of LFIA based on AuNPs and high-entropy alloys

To evaluate the sensitivity of AuNPs- and high-entropy alloys (HEAs)-based LFIA for *S. aureus* detection, standard *S. aureus* suspensions were tested under optimized conditions. Standard *S. aureus* suspensions with concentrations ranging from 1.5×10^5 to 15×10^8 CFU/mL for AuNPs-based LFIA and from 1.5×10^1 to 9×10^8 CFU/mL for HEAs-based LFIA in PB solution were tested. The PB solution served as the negative control. To minimize false-positive results, the cutoff value was set at 99.9 without DAB and 254.5 with DAB (Mean + 3SD). As shown in Fig. 6A, no color was observed on the T-line for negative samples, with T-line signal intensities near zero. For positive samples, T-line color intensity progressively increased with rising *S. aureus* concentrations. As illustrated in Fig. 6D, the red band intensity on the T-line was directly proportional to the logarithm of *S. aureus* concentration, described by $y = -788.36 + 176.37 \lg x$ ($R^2 = 0.977$), where x represents the concentration of *S. aureus* and y represents the intensity of the test line. Based on visual assessment, the detection limit for AuNPs-LFIA was approximately 1.5×10^6 CFU/mL (Fig. 6A). The intensities for HEAs-LFIA also showed strong linear correlations with the logarithm of *S. aureus* concentration, represented as $y = 120.48 + 40.95 \lg x$ ($R^2 = 0.988$, Fig. 6F) and $y = -816.5 + 159.8 \lg x$ ($R^2 = 0.977$, Fig. 6E). Additionally, the colorimetric signal generated by catalysis displayed a linear relationship with the logarithm of *S. aureus* concentration, expressed as $y = 395.63 + 68.06 \lg x$ ($R^2 = 0.953$, Fig. 6H) and $y = 3.94 + 107.34 \lg x$ ($R^2 = 0.993$, Fig. 6G). The detection limits for HEAs-LFIA and DAB-enhanced HEAs-LFIA were approximately 1.5×10^3 CFU/mL (Fig. 6B) and 15 CFU/mL (Fig. 6C), respectively. These results demonstrated significant potential for field assays and rapid screening without the need for additional instrumentation. This makes the HEAs-LFIA, particularly the

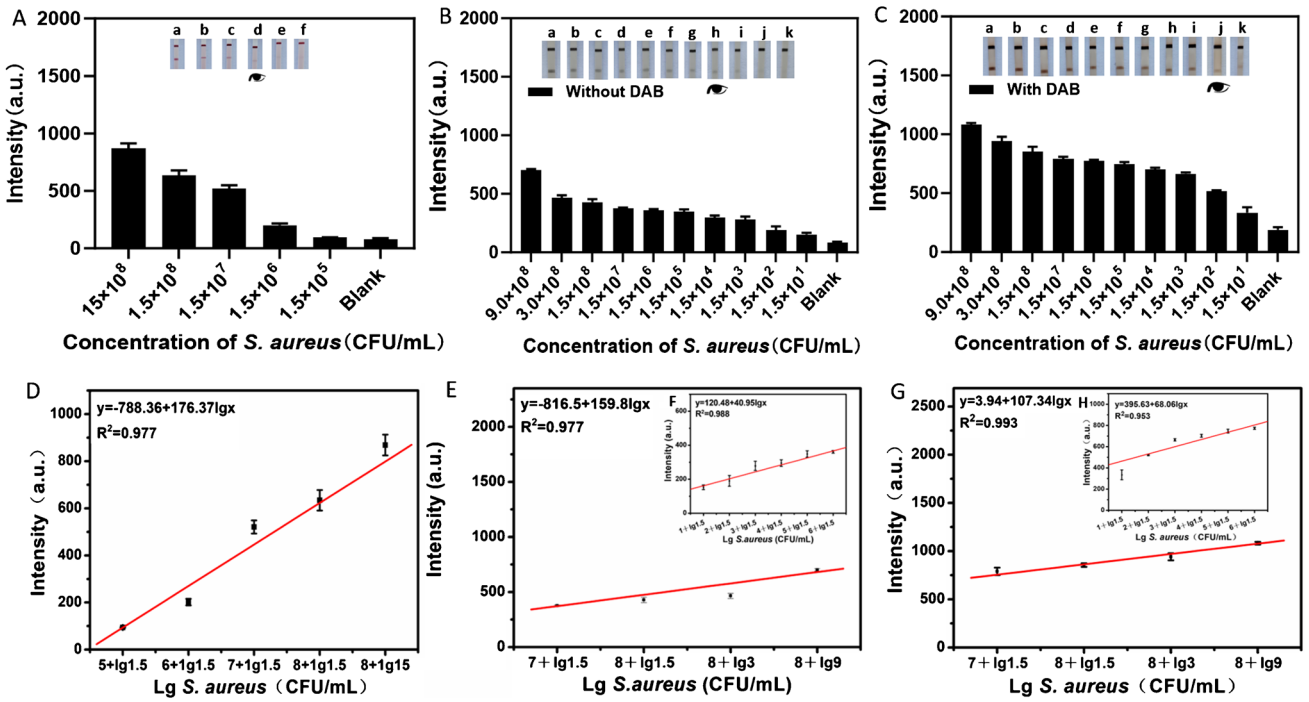

Fig. 6 Investigation of sensitivity. **A** AuNPs-LFIA strip results at various concentrations of *S. aureus* and corresponding color intensity, (a: 15×10^8 CFU/mL; b: 1.5×10^8 CFU/mL; c: 1.5×10^7 CFU/mL; d: 1.5×10^6 CFU/mL; e: 1.5×10^5 CFU/mL; f: Blank). **B** and **C** HEAs-LFIA strip at different *S. aureus* concentrations with corresponding color intensity and catalytic signals, (a: 9×10^8 CFU/mL; b:3×10^8 CFU/mL; c: 1.5×10^8 CFU/mL; d: 1.5×10^7 CFU/mL; e: 1.5×10^6 CFU/mL; f: 1.5×10^5 CFU/mL; g: 1.5×10^4 CFU/mL; h: 1.5×10^3 CFU/mL; i: 1.5×10^2 CFU/mL; j: 1.5×10^1 CFU/mL; k: Blank). **D** Calibration curves of T-line intensity versus the logarithm of *S. aureus* concentration. **E** Standard curves prior to catalysis. **F** Standard curves post-catalysis

DAB-enhanced test, a promising tool for highly sensitive and portable detection of *S. aureus*.

Specificity and stability of LFIA based on high-entropy alloys

The specificity of the HEAs-LFIA was evaluated by testing it against several potential interfering organisms, including *S. epidermidis*, *E. coli*, *P. aeruginosa*, *E. faecium* (Fig. S1 and Fig. S2). As shown in Fig. 7A, only *S. aureus* produced a signal response in the HEAs-LFIA and DAB-enhanced HEAs-LFIA, while other bacteria were virtually undetectable. These findings confirmed the excellent specificity of HEAs-LFIA. Storage stability, an essential factor for LFIA test strips, was also evaluated. The test strips were stored in a desiccator at room temperature, and the strips were tested again four weeks later. As illustrated in Fig. 7B, the strips maintained a clear and consistent response to the target bacteria, with no significant changes in the T-line signal intensity. These results demonstrated that the test strips exhibited good stability under general storage conditions.

Detection of S. aureus in food samples using HEAs-based LFIA

To evaluate the practical applicability of the proposed HEAs-based LFIA test strips, they were applied for rapid bacterial detection in milk and orange juice samples (Fig. S3). Pretreated sample solutions were mixed with labeled probes and analyzed using the test strips. Quantitative assessments were performed using the previously established linear working curves. As summarized in Table 1, no *S. aureus* was detected in the selected milk and orange juice samples. To investigate the repeatability in food samples, five identical probe-HEAs nanozymes were prepared and measured individually in separate solutions containing 9×10^8 CFU/mL of the target bacteria [44, 45].

Table 1 Real sample assay for *S. aureus* detection using HEAs-based LFIA test strips ($n = 5$)

Sample	*S. aureus* concentration ($\times 10^8$ CFU/mL)				
	Measured	Spiked	Measured	RSD (%)	Recovery (%)
Milk	undetectable	9.0	9.20	8.1	102.2
Orange juice	undetectable	9.0	10.62	7.3	118.0

The study demonstrated satisfactory repeatability, with a low relative standard deviation (RSD) in milk (8.1%, $n = 5$) and orange juice (7.3%, $n = 5$). No significant change was observed, $t_{calculated} = 2.57 < t_{critical,4} = 2.78$ and $t_{calculated} = 2.02 < t_{critical,4} = 2.78$, with a desirable recovery of 102.2% and 118.0%, respectively. Additionally, interday variability (over 5 days, Table S2) and intraday variability (five measurements within a single day, Table S1) were assessed by recording the signal response of the probe-HEAs nanozymes in the presence of target bacteria at a concentration of 1.5×10^6 CFU/mL [46, 47]. The observed |t| values for intraday and interday measurements (0.781 and 1.195, respectively) were both lower than the critical value at $P = 0.05$ ($|t|_{Critical,4} = 2.78$), confirming that there was no evidence of systematic error.

We also summarized the recently published results for various pathogen detection by different LFIAs (Table 2). The comparison results revealed that the assay performance of the HEAs-based LFIA could match or exceed those previously reported LFIAs for pathogen detection. These results demonstrate that the proposed HEAs-based LFIA exhibits strong tolerance to matrix interference and high quantitative precision. The findings confirm that the HEAs-based LFIA test strips offer substantial potential for on-site, accurate, and rapid bacterial detection in food samples, making them suitable for practical applications in food safety monitoring.

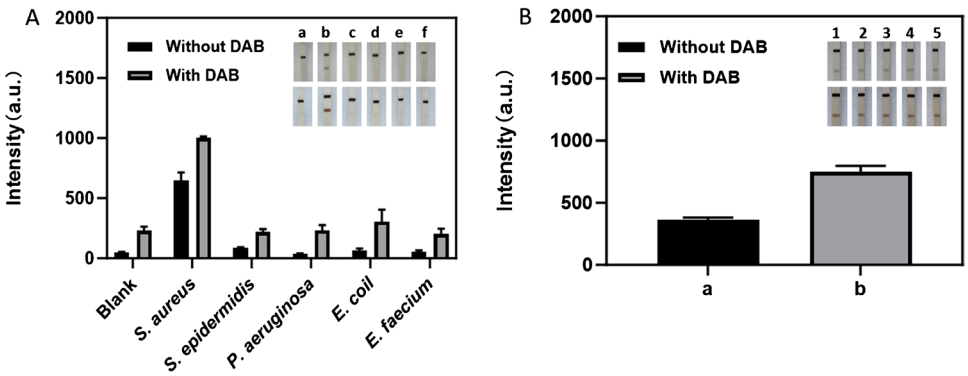

Fig. 7 **A** Specificity evaluation of HEAs-LFIA against various interfering bacterial strains, (a: Blank; b: *S. aureus* ATCC 29213; c: *S. epidermidis*; d: *P. aeruginosa*; e: *E. coli*; f: *E. faecium*). **B** Stability assessment of HEAs-based LFIA test strips after 4 weeks of storage under standard conditions. Error bars indicate ± SD from five independent measurements

Table 2 Comparison of the sensitivity of different LFIA biosensors for pathogen detection

Detection method	Type of label	LoD (CFU/mL)	Reference
LFIA	Au/Ir@Cu/Zn-MOF	10^3	[48]
Colorimetric	SapYZUM13@Mn_3O_4-NH_2	20	[49]
Electrochemical	MXene@Au	38	[50]
Colorimetric	Silver	2×10^2	[51]
Photothermal/Colorimetric	Ag–Au urchin-like hollow nanospheres	5.50×10^2/2.48×10^3	[52]
SERS/Photothemal/Colorimetric	Au − Ag@Pt nanoparticles	3/27/18	[53]
LFIA	HEAs	15	This work

Conclusion

In conclusion, we successfully synthesized the ultrasmall high-entropy alloys via a low-temperature reduction-diffusion strategy and integrated them into the LFIA for the sensitive detection and specific discrimination of *Staphylococcus aureuss*. Compared to the catalytic kinetic performance of AuNPs, Au-PtNPs, Au-Pt-IrNPs, Au-Pt-Ir-RuNPs, HEAs exhibited high catalytic activity. These results indicated that HEAs hold significant potential as a high-performance label for signal amplification on the LFIA platform. The LoD for *S. aureus* reached 1.5×10^3 and 15 CFU/mL with HEAs-LFIA and DAB-enhanced HEAs-LFIA, which exceeded those of conventional AuNPs-based LFIA by 10^3- and 10^5-fold. Moreover, the recoveries of *S. aureus* in milk and orange juice were 102.2% and 118.0%, demonstrating good applicability for real sample analysis. This work underscores the potential of HEAs-based LFIA as a versatile and robust platform for the on-site detection of *S. aureus* and other foodborne pathogens, offering a promising new technological approach for food safety monitoring and pathogen detection in practical applications.

Supplementary Information The online version contains supplementary material available at https://doi.org/10.1007/s00604-025-07213-x.

Acknowledgements This work was supported by grants from National Natural Science Foundation of China (82160026) and grants from Guizhou Provincial Science & Technology Department (gzsyqcc(2023)010, gpph-nsfc-2021-6, qkhptrc2018-5636-2, qkhjc-zk(2021)492, and qkhcg2023-ZD010).

Author contributions Wei huang: Original Draft, Formal analysis, Review. Zhen Ren: Formal analysis, Methodology, Software. Xukui Li: Methodology, Software. Rong Chen: Software, Conceptualization. Dinglin Fan: Data curation, Methodology. Jingjing Da: Data curation, Investigation. Yan Zha: Resources, Formal analysis. Yongjie Xu: Funding acquisition, and editing, Validation.

Funding This work was supported by grants from National Natural Science Foundation of China (82160026) and grants from Guizhou Provincial Science & Technology Department (gzsyqcc(2023)010, gpph-nsfc-2021–6, qkhptrc2018-5636–2, qkhjc-zk(2021)492, and qkhcg2023-ZD010).

Data availability No datasets were generated or analysed during the current study.

Declarations

Competing interests The authors declare no competing interests.

References

1. Borsa BA, Tuna BG, Hernandez FJ et al (2016) *Staphylococcus aureus* detection in blood samples by silica nanoparticle-oligonucleotides conjugates. Biosens Bioelectron 86:27–32
2. Suaifan GA, Alhogail S, andM Zourob, (2017) Rapid and low-cost biosensor for the detection of *Staphylococcus aureus*. Biosens Bioelectron 90:230–237
3. Zhao M, Yao X, Liu S et al (2021) Antibiotic and mammal IgG based lateral flow assay for simple and sensitive detection of *Staphylococcus aureus*. Food Chem 339:127955
4. Rubab M, Shahbaz HM, Olaimat AN et al (2018) Biosensors for rapid and sensitive detection of *Staphylococcus aureus* in food. Biosens Bioelectron 105:49–57
5. Yang Y, Wang S-Q, Wen H et al (2019) Nanoporous gold embedded ZIF composite for enhanced electrochemical nitrogen fixation. Angew Chem Int Ed 58(43):15362–15366
6. Chang RYK, Nang SC, Chan HK et al (2022) Novel antimicrobial agents for combating antibiotic-resistant bacteria. Adv Drug Deliv Rev 187:114378
7. Ma Y, Wei H, Wang Y et al (2024) Efficient magnetic enrichment cascade single-step RPA-CRISPR/Cas12a assay for rapid and ultrasensitive detection of *Staphylococcus aureus* in food samples. J Hazard Mater 465:133494
8. Roberts A, Prakashan D, Dhanze H et al (2022) Immuno-chromatic probe based lateral flow assay for point-of-care detection of Japanese encephalitis virus NS1 protein biomarker in clinical samples using a smartphone-based approach. Nanoscale Advances 4(18):3966–3977
9. Jampasa S, Kreangkaiwal C, Kalcher K et al (2022) resistance-based lateral flow immunosensor with a NFC-enabled smartphone for rapid diagnosis of Leptospirosis in clinical samples. Anal Chem 94(42):14583–14592
10. Prakashan D, Shrikrishna NS, Byakodi M et al (2022) Gold nanoparticle conjugate-based lateral flow immunoassay (LFIA) for rapid detection of RBD antigen of SARS-CoV-2 in clinical samples using a smartphone-based application. J Med Virol 95(1)

11. Mahari S, Prakashan D, andS Gandhi, (2023) Immunochromatographic assay for the point-of-care diagnosis of food borne *Salmonella* strains using smartphone application. Colloids Surf B Biointerfaces 226:113319
12. Tang Y, Yao L, Wang Y et al (2025) Signal-on lateral flow immunoassays for rapid detection of tetrodotoxin in pufferfish. J Hazard Mater 486:136973
13. Prakashan D, Kolhe P, andS Gandhi, (2024) Design and fabrication of a competitive lateral flow assay using gold nanoparticle as capture probe for the rapid and on-site detection of Penicillin antibiotic in food samples. Food Chem 439:138120
14. Wang W, Liu L, Song S et al (2015) A highly sensitive ELISA and immunochromatographic strip for the detection of Salmonella typhimurium in milk samples. Sensors (Basel) 15(3):5281–5292
15. Wen-de W, Min L, Ming C et al (2017) Development of a colloidal gold immunochromatographic strip for rapid detection of Streptococcus agalactiae in tilapia. Biosens Bioelectron 91:66–69
16. Huang L, Jin J, Ao L et al (2020) Hierarchical plasmonic-fluorescent labels for highly sensitive lateral flow immunoassay with flexible dual-modal switching. ACS Appl Mater Interfaces 12(52):58149–58160
17. Wang J, Jiang C, Jin J et al (2021) Ratiometric fluorescent lateral flow immunoassay for point-of-care testing of acute myocardial infarction. Angew Chem Int Ed Engl 60(23):13042–13049
18. Suryoprabowo S, Liu L, Kuang H et al (2021) Fluorescence based immunochromatographic sensor for rapid and sensitive detection of tadalafil and comparison with a gold lateral flow immunoassay. Food Chem 342:128255
19. Abbaspour A, Norouz-Sarvestani F, Noori A et al (2015) Aptamer-conjugated silver nanoparticles for electrochemical dual-aptamer-based sandwich detection of *Staphylococcus aureus*. Biosens Bioelectron 68:149–155
20. Wen C-Y, Zhao L-J, Wang Y et al (2023) Colorimetric and photothermal dual-mode lateral flow immunoassay based on Au-Fe_3O_4 multifunctional nanoparticles for detection of *Salmonella typhimurium*. Microchimica Acta 190(2)
21. Guo D, Li H, Zhang Y et al (2024) A multifunctional MOF-on-MOF-based dual-channel luminescent signal readout strategy for classifying phenylglyoxylic acid and 2,6-dipicolinic acid. Cryst Growth Des 24(12):5251–5262
22. Liu H, Dai E, Xiao R et al (2021) Development of a SERS-based lateral flow immunoassay for rapid and ultra-sensitive detection of anti-SARS-CoV-2 IgM/IgG in clinical samples. Sens Actuators, B Chem 329:129196
23. Liu S, Liao Y, Shu R et al (2024) Evaluation of the multidimensional enhanced lateral flow immunoassay in point-of-care nanosensors. ACS Nano 18(40):27167–27205
24. Yao L, Zhang F, Yang S et al (2024) Sub-2 nm IrRuNiMoCo high-entropy alloy with iridium-rich medium-entropy oxide shell to boost acidic oxygen evolution. Adv Mater 36(25):2314049
25. El-Atwani O, Li N, Li M et al (2019) Outstanding radiation resistance of tungsten-based high-entropy alloys. Sci Adv 5(3):eaav2002
26. Li Z, Pradeep KG, Deng Y et al (2016) Metastable high-entropy dual-phase alloys overcome the strength-ductility trade-off. Nature 534(7606):227–230
27. Praveen S, Kim HS (2018) High-entropy alloys: potential candidates for high-temperature applications – an overview. Adv Eng Mater 20(1):1700645
28. Li H, Lai J, Li Z et al (2021) Multi-sites electrocatalysis in high-entropy alloys. Adv Func Mater 31(47):2106715
29. Liao Y, Li Y, Zhao R et al (2022) High-entropy-alloy nanoparticles with 21 ultra-mixed elements for efficient photothermal conversion. Natl Sci Rev 9(6):nwac041
30. Ma Y, Ma Y, Wang Q et al (2021) High-entropy energy materials: challenges and new opportunities. Energy Environ Sci 14(5):2883–2905
31. Ren J, Zhang Y, Zhao D et al (2022) Strong yet ductile nanolamellar high-entropy alloys by additive manufacturing. Nature 608(7921):62–68
32. Zhu Z, Jiang T, Ali M et al (2022) Rechargeable batteries for grid scale energy storage. Chem Rev 122(22):16610–16751
33. Ai Y, He M-Q, Sun H et al (2023) Ultra-small high-entropy alloy nanoparticles: Efficient nanozyme for enhancing tumor photothermal therapy. Adv Mater 35(23):2302335
34. Jung SG, Han Y, Kim JH et al (2022) High critical current density and high-tolerance superconductivity in high-entropy alloy thin films. Nat Commun 13(1):3373
35. Cantor B, Chang ITH, Knight P et al (2004) Microstructural development in equiatomic multicomponent alloys. Mater Sci Eng, A 375–377:213–218
36. Yeh JW, Chen SK, Lin SJ et al (2004) Nanostructured high-entropy alloys with multiple principal elements: novel alloy design concepts and outcomes. Adv Eng Mater 6(5):299–303
37. Xin Y, Li S, Qian Y et al (2020) High-entropy alloys as a platform for catalysis: progress, challenges, and opportunities. ACS Catal 10(19):11280–11306
38. Yao Y, Dong Q, Brozena AH et al (2022) High-entropy nanoparticles: synthesis-structure-property relationships and data-driven discovery. Science 376
39. Batchelor TAA, Pedersen JK, Winther SH et al (2019) High-entropy alloys as a discovery platform for electrocatalysis. Joule 3(3):834–845
40. Li X, Lu L, Li J et al (2020) Mechanical properties and deformation mechanisms of gradient nanostructured metals and alloys. Nat Rev Mater 1–18
41. Yi YN, Ni YX, Zhang JN et al (2024) Research progress of high-entropy alloy catalysts in water electrolysis for hydrogen production and hydrogen fuel cells. Low-Carbon Chem Chem Eng 49(9)
42. Ji X, Song X, Li J et al (2007) Size control of gold nanocrystals in citrate reduction: the third role of citrate. J Am Chem Soc 129(45):13939–13948
43. Jiang B, Duan D, Gao L et al (2018) Standardized assays for determining the catalytic activity and kinetics of peroxidase-like nanozymes. Nat Protoc 13(7):1506–1520
44. Khoshfetrat SM, Fasihi K, Moradnia F et al (2023) A label-free multicolor colorimetric and fluorescence dual mode biosensing of HIV-1 DNA based on the bifunctional NiFe2O4@UiO-66 nanozyme. Analytica Chimica Acta 1252
45. Khoshfetrat SM, Motahari M, Mirsian S (2025) 3D porous structure of ionic liquid-delaminated Ti3C2 MXene nanosheets for enhanced electrochemical sensing of tryptophan in real samples. Sci Rep 15(1)
46. Khoshfetrat SM, Mamivand S, Darband GB (2024) Hollow-like three-dimensional structure of methyl orange-delaminated Ti3C2 MXene nanocomposite for high-performance electrochemical sensing of tryptophan. Microchimica Acta 191(9)
47. Mehdi Khoshfetrat S, Moradi M, Zhaleh H et al (2024) Multifunctional methyl orange-delaminated Ti3C2 MXene for non-enzymatic/metal-free electrochemical detection of hydrogen peroxide and hydrazine. Microchem J 205
48. Zhong Y, Zheng XT, Li Q-l et al (2023) Antibody conjugated Au/Ir@Cu/Zn-MOF probe for bacterial lateral flow immunoassay and precise synergistic antibacterial treatment. Biosens Bioelectron 224:115033
49. Han Y, Zhou W, Wu Y et al (2024) Characterisation of a colourimetric biosensor SapYZUM13@Mn3O4-NH2 reveals the mechanisms underlying its rapid and sensitive detection of viable *Staphylococcus aureus* in food. Food Chem 457:140189

50. Li W, Bai X, Xiao F et al (2023) MXene@Au based electrochemical biosensor with pretreatment by magnetic nanoparticles for determination of MRSA from clinical samples. J Hazard Mater 457:131823
51. Panferov VG, Safenkova IV, Varitsev YA et al (2016) Development of the sensitive lateral flow immunoassay with silver enhancement for the detection of Ralstonia solanacearum in potato tubers. Talanta 152:521–530
52. Zhang G, Hu H, Deng S et al (2023) An integrated colorimetric and photothermal lateral flow immunoassay based on bimetallic Ag–Au urchin-like hollow structures for the sensitive detection of *E. coli* O157:H7. Biosens Bioelectron 225:115090
53. Huang X, Chen L, Zhi W et al (2023) Urchin-shaped Au–Ag@Pt sensor integrated lateral flow immunoassay for multimodal detection and specific discrimination of clinical multiple bacterial infections. Anal Chem 95(35):13101–13112